Methods

Vendor's calibration

The calibration and preparation methods used by various manufacturers in the United States are similar. Each seed is placed in a dose calibrator of fixed geometry. The sources are then grouped in subsets, each having an air-kerma strength variable by ±2%. When an order is received from the customer, it is filled from one to three subsets that have sequential dose calibrations. Therefore, the resultant seed order would have an air-kerma strength value with a potential variability range of up to 5%. This range should be taken into consideration when the QA program is designed. The tolerance for the manufacturer's calibration statement is 5% at most. STM1251 sources have three different air-kerma strengths, 0.378, 0.450, and 0.525 U. Seeds with these air-kerma strengths are imported and commonly used in Japan.

Single-seed assay

Thirty-four prostate cancer patients were treated with a permanent prostate implant using ^{125}I seeds. All of them were classified as low-risk patients, with an initial prostate-specific antigen level of less than 10 ng/ml, Gleason score 6 or less, and T classification T2a or less (International Union Against Cancer [Unio Internationalis Contra Cancrum (UICC)] 2002).[15] The air-kerma strength used was 0.450 U for all cases. Most of the verification was performed on a Monday at our department, while in some cases the measurement was performed on Tuesday or Wednesday of the same week, when the air-kerma strength had to be modified in accordance with the decay. A total of 2412 seeds were measured.

Single-seed assays were performed using a reentrant-type ionization chamber (CRC-15BT Dose Calibrator; Capintec, Ramsey, NJ, USA) and an adapted source holder that assures reproducible source geometry and minimal absorption. The chamber calibration for ^{125}I seeds (model STM1251) was acquired from an accredited dosimetry calibration laboratory (ADCL) and was subsequently checked with an ADCL-calibrated ^{125}I seed. Agreement between the chamber and source was within 1%, which means that direct traceability is established when a well chamber is calibrated against a national standard at an ADCL. The chamber has a sealed thin wall, and features a deep well design with low-pressure Argon gas and a 500-V bias in order to achieve optimal response time (within 2 s) without temperature or pressure corrections. Source activity can be measured accurately in either Curie (Ci) or air-kerma strength (U). Because sources measured are inside the vial bottle without being sterilized, all sources should be sterilized after the single-seed assay.

Data analysis

The measured data were entered onto a spreadsheet (Excel; Microsoft, Redmond, WA, USA), which contained a simple macro written to analyze the data. These data consisted of the minimum, maximum, mean, median, and SD values. For each of the 34 patients entered in this study we verified whether the discrepancy between the mean measured value and the manufacturer's stated value was less than 3%, and we also verified that the difference between the actual measured value for each seed and the mean measured value was less than 5%. These tolerances were based on the recommendations of the TG-56.[10]

Using the data for the discrepancies between the mean measured values and the manufacturer's stated value for all cases, a histogram was created with a range of −5% to +5%.

Results

Only 16 of the total of 2412 seeds (0.66 %) displayed a more than 5% difference between the measured value and the manufacturer's stated value (Table 1). The tolerance of disagreement for the recommendation of the TG-56[10] was less than 1%. In none of the cases did more than 3 seeds exceed the tolerance of 5% against the manufacturer's stated value, as shown in Table 1. Figure 1 shows the frequency histogram for the model STM1251 source expressed as the discrepancies between the measured mean value and the manufacturer's stated value. The disagreement ranged from −2% to 5% (median, 1%). In each case the SD from the mean value ranged from 1.1% to 2.5 % (median, 2.2%). In 3 of the total of 34 patients (9%), the tolerance exceeded the limit of 3% recommended by the TG-40.[9] However, agreement between the stated source strength and our measurements was within the manufacturer's calibration tolerance (±5%).

Discussion

In 1979, The Radiological Physics Center discovered a systematic discrepancy in the calibration of source strength of ^{125}I seeds.[16] Although manufacturers claimed to have

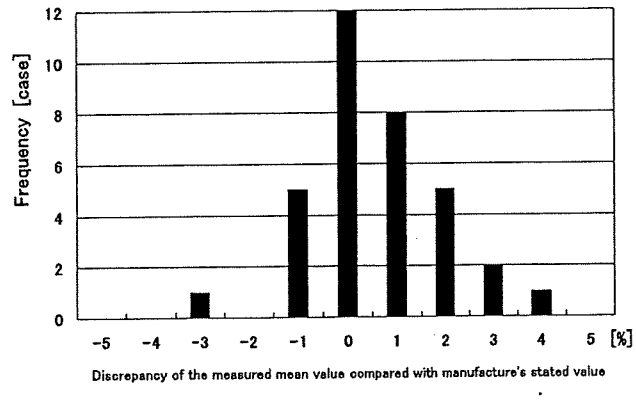

Fig. 1. Histogram of discrepancies between measured mean values and manufacturer's stated value. *Frequency* shows number of cases

Table 1. Data analysis of source strength showing the number of seeds used for implant, the number of seeds exceeding 5% tolerance, and the discrepancies between the measured mean value and the manufacturer's stated value

Case no.	Seed count	Number of seeds with more than 5% discrepancy between source strength and mean value	Mean value minus manufacturer's stated value (%)
1	79	0	0.58
2	60	0	1.41
3	58	2	0.00
4	80	2	0.28
5	90	1	0.28
6	75	3	−0.85
7	110	0	1.13
8	95	1	0.85
9	65	1	−0.57
10	65	2	3.94
11	83	2	2.25
12	60	0	1.69
13	110	0	0.85
14	90	0	4.79
15	65	0	1.99
16	46	0	2.82
17	98	1	0.85
18	71	0	0.56
19	68	0	1.97
20	99	0	2.54
21	84	0	1.97
22	61	1	2.82
23	62	0	−2.54
24	48	0	−0.28
25	90	0	3.10
26	73	0	2.25
27	39	0	1.41
28	75	0	0.56
29	45	0	0.85
30	35	0	1.99
31	45	0	0.28
32	50	0	0.56
33	73	0	−0.28
34	65	0	0.56

checked and verified the source strength of every seed before supplying them, it was found that seeds without radioactivity, or with radioactivity other than the supposed source strength may have been included in the supply. For this reason, the AAPM recommends that the manufacturer's assay must be independently confirmed by the institution's medical physicist. The United States has set a good example, because this recommendation has been adopted by some state and federal regulatory bodies[12] and by professional organizations such as the American College of Radiology (ACR),[17,18] the American Brachytherapy Society (ABS),[19] and the American College of Medical Physics (ACMP).[13] In stark contrast with the situation in the United States, a single-seed assay has not been performed at any institution in Japan. In addition, because there are rather few medical physicists in Japan, it should be noted that the QA for radiation therapy may not be satisfactory. At the moment there is no air-kerma strength standard for ^{125}I seeds in Japan, so that we have to send the ionization chamber to an ADCL to obtain the calibration factor of the air-kerma strength standard for the ^{125}I seeds. This can take as long as 2 months and can be very expensive. Moreover, the form in which the source is supplied, at least in Japan, tends to shift between a nonsterilized vial and a sterilized cartridge. If a single-seed assay is performed under sterile conditions, one should pay careful attention to keep the inner wall of the well-type ionization chamber sterilized during the procedure.

According to the AAPM TG-56,[10] every institution practicing brachytherapy should have a system in place to assure secondary traceability for all source types used in its practice. Single-seed assays are performed routinely at every such institution in countries other than Japan. Because the type of ionization chamber used in our study needs no temperature or pressure corrections and its response time is within 2 s, it takes only around 40 min to measure all seeds for one patient. Very few medical physicists, only about 30, are working in hospitals in Japan. Because 90 institutions have started using permanent prostate implants,[20] it is very difficult for these medical physicists to verify and check the source strength at every institution. However, it is imperative that the verification of source strength be continued, so that it may well be necessary to increase the number of medical physicists.

In the present study we have indicated that every institution should take responsibility for performing a single-seed assay every implant. In the United States, medical physicists are responsible for correctly delivering the dose prescribed by a physician, so that the cost of the medical services is covered under the Cur-rent Procedural Terminology (CPT) billing code number 77331, special dosimetry.

When the discrepancy between the mean measured value and the manufacturer's stated value was more than 3% or the deviation from the mean measured value was more than 5%, we have reported our findings to the manufacturer after checking whether the measurement procedure had been performed correctly. These procedures were followed in accordance with the recommendations of the AAPM Low-Energy Brachytherapy Source Calibration Working Group.[19] However, because medical physicists are not licensed on a national basis in Japan, it may be difficult to employ a medical physicist at every institution. We therefore strongly hope that governmental certification of medical physicists is established as soon as possible.

Conclusion

A single-seed assay was performed for use of the model STM1251 seed in 34 cases. The total number of seeds was 2412. The manufacturer's stated strength of the ^{125}I seeds agreed well with the measured value. Our study proved to be helpful as a guide for the use of permanent prostate implants of the model STM1251 seed.

Conflict of interest statement

No author has any conflict of interest.

Acknowledgments The authors wish to thank Medicon Corporation for providing us with opportunities to measure the source strength at various institutions.

References

1. Kirov AS, Williamson JF (2001) Monte Carlo-aided dosimetry of the Source Tech Medical Model STM1251 I-125 interstitial brachytherapy source. Med Phys 28:764–772
2. Lee PC, Starr SJ, Zuhlke K, et al. (1999) Comparison of a proposed five-seed assay method with the single-seed and batch assay methods for I-125 seeds in ultrasound-guided prostate implants. Radiat Oncol Investig 7:374–381
3. Mellenberg DE, Kline RW (1995) Verification of manufacturer-supplied 125I and 103Pd air-kerma strengths. Med Phys 22: 1495–1497
4. DeWerd LA (1997) Brachytherapy dosimetric assessment: source calibration. In: Thomadsen B (ed) Categorical course in brachytherapy physics syllabus. Radiological Society of North America, Oak Brook, IL, pp 143–153
5. Hanson WF, Shalek RJ, Kennedy P (1991) Dosimetry quality assurance in the U.S. from the experience of the Radiological Physics Center. In: Starkschall G, Horton J (eds) Proceedings of an American College of Medical Physics Symposium: quality assurance in radiotherapy physics. Medical Physics Publishing, Madison, WI, pp 255–282
6. DeWerd LA, Thomadsen BR (1995) American Association of Physicists in Medicine 1994 Summer School Proceedings Brachytherapy Physics. In: Williamson JF, Thomadsen BR, Nath R (eds) Medical Physics Publishing, Madison, WI
7. DeWerd LA (2005) American Association of Physicists in Medicine 2005 Summer School Proceedings Brachytherapy Physics, Monograph No. 31. Thomadsen BR, Rivard MJ, Butler WM (eds) Medical Physics Publishing, Madison, WI, pp 153–171
8. DeWerd LA (1997) Brachytherapy dosimetric assessment: source calibration. In: Thomadsen BR (ed) Syllabus of categorical course in brachytherapy physics. Radiological Society of North America, Oak Brook, IL, pp 143–153
9. Kutcher GJ, Coia L, Gillin M, et al. (1994) Comprehensive QA for radiation oncology: report of AAPM Radiation Therapy Committee Task Group 40. Med Phys 21:581–681
10. Nath R, Anderson LL, Meli JA, et al. (1997) Code of practice for brachytherapy physics: report of the AAPM Radiation Therapy Committee Task Group No. 56. Med Phys 24:1557–1598
11. Yu Y, Anderson LL, Li Z, et al. (1999) Permanent prostate seed implant brachytherapy: report of the American Association of Physicists in Medicine Task Group No.64. Med Phys 26: 2054–2076
12. US Nuclear Regulatory Commission (2002) Code of Federal Regulations, 10 CFR 35.432 and 10 CFR 35.630. Washington, DC, Federal Register, 67(79)
13. Butler WM, Bice WS, DeWerd LA, et al. (2008) Third-party brachytherapy source calibrations and physicist responsibilities: report of the AAPM Low Energy Brachytherapy Source Calibration Working Group. Med Phys 35:3860–3865
14. Takahashi Y, Ito A, Sumida I et al. (2006) Dosimetric consideration of individual ^{125}I source strength measurement and a large-scale comparison of that measured with a nominal value in permanent prostate implant brachytherapy. Radiat Med 24: 675–679
15. Sobin LH, Wittekind CH (2002) UICC: TNM classification of malignant tumors. 6th edn. Wiley-Liss, New York
16. Starkschall G, Horton JL (1991) Quality assurance in radiotherapy physics. Medical Physics Publishing, Madison, WI, pp 263–266
17. American College of Radiology (2006) Practice guideline for transperineal permanent brachytherapy of prostate cancer. ACR Practice Guidelines. ACR, pp 909–915
18. American College of Radiology (2006) ACR technical standard for the performance of brachytherapy physics: manually loaded temporary implants. ACR Practice Guidelines. ACR, pp 1119–1123
19. Rivard MJ, Butler WM, Devlin PM, et al. (2007) American Brachytherapy Society recommends no change for prostate permanent implant dose prescriptions using iodine-125 or palladium-103. Brachytherapy 6:34–37
20. Yoshioka Y (2009) Current status and perspectives of brachytherapy for prostate cancer. Int J Clin Oncol 14:31–36

Dose profile measurement using an imaging plate: Evaluation of filters using Monte Carlo simulation of 4 MV x-rays

Masatoshi Hashimoto,[1,2,a)] Tetsuya Tomita,[3] Koichi Sawada,[3] Toshioh Fujibuchi,[4] Teiji Nishio,[5] and Keiichi Nakagawa[1]

[1]*Division of Radiology and Biomedical Engineering, Graduate School of Medicine, The University of Tokyo, Bunkyo-ku, Tokyo 113-8655, Japan*

[2]*Department of Therapeutic Radiology, Medical Plaza Edogawa, Edogawa-ku, Tokyo 133-0052, Japan*

[3]*Department of Radiology, Chiba University Hospital, Cyuo-ku, Chiba 260-8677, Japan*

[4]*Department of Radiological Sciences, School of Health Science, Ibaraki Prefectural University, Inashiki-gun, Ibaraki 300-0394, Japan and Graduate School of Comprehensive Human Sciences, University of Tsukuba, Tsukuba-shi, Ibaraki 305-8575, Japan*

[5]*Particle Therapy Division, Research Center for Innovation Oncology, National Cancer Center Hospital East, Kashiwa-shi, Chiba 277-8577, Japan*

(Received 1 December 2008; accepted 1 March 2009; published online 7 April 2009)

Computed radiography (CR) is gradually replacing film. The application of CR for two-dimensional profiles and off-axis ratio (OAR) measurement using an imaging plate (IP) in a CR system is currently under discussion. However, a well known problem for IPs in dosimetry is that they use high atomic number (Z) materials, such as Ba, which have an energy dependency in a photon interaction. Although there are some reports that it is possible to compensate for the energy dependency with metal filters, the appropriate thicknesses of these filters and where they should be located have not been investigated. The purpose of this study is to find the most suitable filter for use with an IP as a dosimetric tool. Monte Carlo simulation (Geant4 8.1) was used to determine the filter to minimize the measurement error in OAR measurements of 4 MV x-rays. In this simulation, the material and thickness of the filter and distance between the IP and the filter were varied to determine most suitable filter conditions that gave the best fit to the MC calculated OAR in water. With regard to changing the filter material, we found that using higher Z and higher density material increased the effectiveness of the filter. Also, increasing the distance between the filter and the IP reduced the effectiveness, whereas increasing the thickness of the filter increased the effectiveness. The result of this study showed that the most appropriate filter conditions consistent with the calculated OAR in water were the ones with the IP sandwiched between two 2 mm thick lead filters at a distance of 5 mm from the IP or the IP sandwiched directly between two 1 mm lead filters. Using these filters, we measured the OAR at 10 cm depth with 100 cm source-to-surface distance and surface 10×10 cm^2 field size. The results of this measurement represented that it is possible to achieve measurements with less than within 2.0% and 2.0% in the field and with less than 1.1% and 0.6% out of the field by using 2 and 1 mm lead filters, respectively. © *2009 American Institute of Physics.* [DOI: 10.1063/1.3103572]

I. INTRODUCTION

For radiation therapy, it is important to measure the dose distribution in materials in order to put together a treatment plan that will give an accurate dose distribution and ensure that the dose to normal tissue is minimized. The usual way to measure this is to use an ion chamber in water as a gold standard. However, because this is a sort of point measurement, it is time-consuming to measure the off-axis ratio (OAR) in two or three dimensions. Furthermore, the resolution of scans is limited due to chamber size.

To measure the dose distribution with high spatial resolution the use of film is an easier solution.[1–4] However, the film needs to be developed, and requires that the film processor be maintained. With GafChromic film,[5–7] it may be much easier and more useful because of no need to be chemical processing; however, all facilities cannot afford to purchase the film digitizer and use such expensive films constantly as a quality assurance tool. On the other hand, computed radiography (CR) system,[8] which has been originally used for diagnostic purpose, has been more widely used than GafChromic film. Additionally, it is being discussed that CR becomes more prevalent in radiotherapy. The use of the film processor is decreasing.

A new dosimetric method using an imaging plate[9,10] (IP) in a CR system has recently been considered as a replacement for film,[11–13] with the advantage that this method does not need a film processor. However, IPs include high atomic number (high Z) materials such as barium, for which there is, in general, an energy dependency problem, which can produce an error in the measurements. It is reported that similar errors occur even in film measurements, but it is possible to

a)Electronic mail: m_hashimoto@movie.ocn.ne.jp.

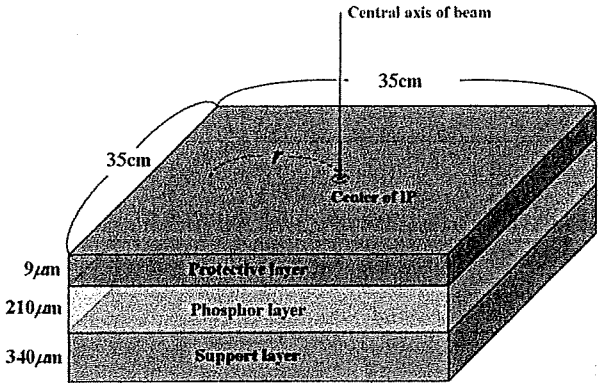

FIG. 1. Structure of the IP used in the MC simulation composed of three layers, a protective layer, a phosphor layer, and a support layer, respectively. *r* is the distance from the center of IP. The center of IP is corresponding to the central axis of x-ray.

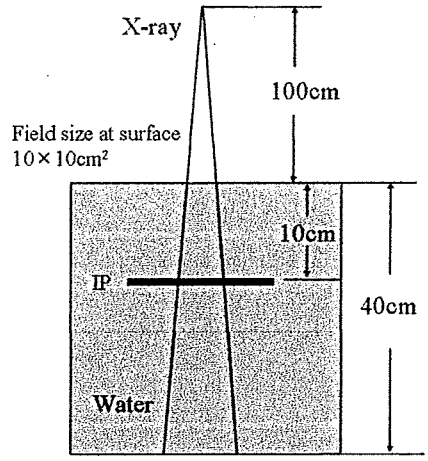

FIG. 2. Materials setting. A $40\times40\times40$ cm^3 water tank phantom was used in the simulation. The SSD was 100 cm and the field size 10×10 cm^2. The middle of water phantom was irradiated with a 4 MV photon beam. The incidence of photons was uniformly carried out in the exposure field. The IP was place at a depth of 10 cm from the surface of water.

compensate these errors with metal filters.[14–16] There has been a report asserting that filters can be used to compensate the errors for IP measurements also.[11] Nevertheless a detailed discussion regarding the kind of materials to use or where the filters should be placed, etc. has not taken place. The purpose of this study is to use Monte Carlo (MC) simulation to determine the most appropriate filter for IP measurements. In this investigation, we attempt to find the most appropriate material, thickness, and location of the filter for IP dosimetry in order to minimize the dosimetric error in OAR measurements with a 4 MV photon beam.

II. MATERIALS AND METHODS

A. MC simulation parameter settings and evaluation

For the MC simulations, we used GEANT4 (version 8.1 patch-01). GEANT4 is a calculation code widely used for high energy physics, nuclear physics, space physics, and medical physics, etc. The photon and electron interactions in the material are simulated down to 250 eV.[17] The GEANT4 physics models selected for this study were the low-energy electromagnetic process, and the number of history was 2×10^8 photons. GEANT4 utilizes a stopping range instead of energy to control the tracking and production of secondaries. In GEANT4, all particles are tracked to a zero range except for secondaries with a range shorter than the production cutoff range set by the user. In this study, the production cutoff range was set to 0.01 mm.

The spectrum used in this study was a 4 MV photon spectrum calculated from Schiff's formula.[18] There have been reports that this formula has been extended for medical linear accelerator.[19–21] In this study, we calculated the spectrum using Schiff's formula, where we attached 10 mm thick copper attenuations by every 50 keV as the target and the material under the target.

The IP used in the MC simulation is a ST-VN (FUJIFILM Corp., Minato-ku, Tokyo). As shown in Fig. 1 the size of the IP is $35\times35\times0.0559$ cm^3 and it is composed of three layers, a protective, phosphor, and support layer and protective and support layers are made of Polyethylene terephthalate (PET), and the phosphor layer is BaFBrI. The composition of PET is C:H:O=10:8:4 and the density is 1.38 g/cm^3. BaFBrI consists of 56.45% Ba, 7.81% F, 27.92% B, 7.82% I, and the density was set to 5.50 g/cm^3. To verify the calculation conditions, we compared measurements and simulation.

1. Measurement

The linear accelerator used was Clinac2100C (Varian Medical Systems Inc., Palo Alto, CA) and we used only 4 MV photons with a 10×10 cm^2 field and a 100 cm source-to-surface distance (SSD). For percentage depth dose (PDD) measurements in water, we used a PTW Freiburg N31005 ionization chamber in a three-dimensional (3D) water phantom (Dynascan, Computerized Medical Systems Inc., St. Louis, MO). We measured the PDD on the central beam axis and the OAR at a depth of 10 cm. For the OAR measurement with the IP, a 40×40 cm^2 water equivalent solid phantom (Solid Water Phantom, Gammex Inc., Middleton, WI) was used instead of the 3D water phantom. The IP (ST-VN, 35×35 cm^2, Fujifilm Corp., Minato-ku, Tokyo) was placed perpendicular to the beam axis at a depth of 10 cm in the stack of 40 cm solid phantom. The IP was exposed to a dose of 12.5 mGy, and was then read out using a FCR5000 (Fujifilm Medical Co. Ltd., Minato-ku, Tokyo) and converted to DICOM format where the *S* value, which gives the sensitivity of the FCR during read out, was set to 2, and the *L* value, which gives the latitude, was set to 4. The other parameter settings were *S*-Shift:1, *C*-Shift:1, GA:A, GC:1.2, GS:0.00, RN:3, RT: F, RE:0.0, and DRC: off. These values were all fixed. The OAR data were obtained from a line profile on the acquired two-dimensional IP dose profiles. To determine the dose deposited on the IP we made the dose conversion table for the pixel value on the IP. First we measured at the central axis with an ion chamber from 2.5 to 15 mGy under the same condition, and next we read out the

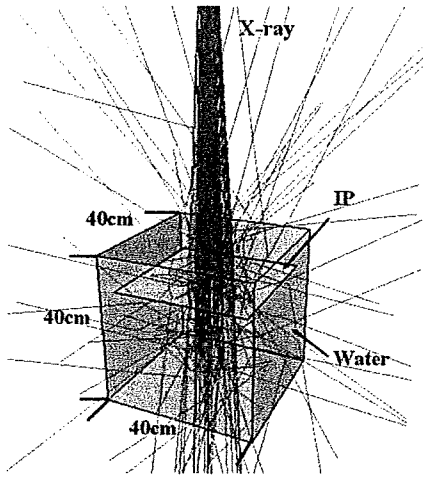

FIG. 3. Example showing the behavior of 100 photons in the water phantom.

corresponding data area on the IP, 100×100 pixels with each pixel being 0.1×0.1 mm^2, and which was compared with the one with ion chamber.

2. MC simulation

The geometrical setup is shown in Fig. 2. First, the PDD and OAR at 10 cm depth were calculated without anything placed in water phantom, where these calculated data were compared with the measured data from the ionization chamber. The voxel size used for the calculation of the water absorbed dose was $5\times5\times5$ mm^3. For the simulation with the IP, the IP was placed perpendicular to the beam axis at a depth of 10 cm, and the OAR was obtained by calculating the dose to the phosphor layer. The voxel size used for this calculation was 5 mm$\times$5 mm$\times$210 μm. Figure 3 is a schematic showing the result of the calculation.

B. Investigating the filter by MC simulation

This calculation also followed the above procedure. The size of filters used in the simulation was 35×35 cm^2, and the filters were set, as shown in Fig. 4, in three different configurations: above only, below only, and one on each side simultaneously. The material, thickness, and displacement of the filters were varied. The same simulation was repeated without the IP and filters, from which the OAR was obtained

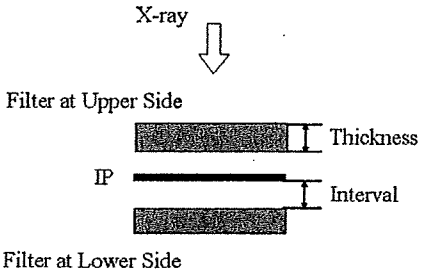

FIG. 4. Schematic diagram showing the location of double filters placed on both sides of the IP. The size of the filter was 35×35 cm^2. The material, thickness, and the distance between the IP and the filter were varied.

and used as a reference for comparison. From the simulation, the appropriate filter was identified as the one for which the calculation result was closest to the OAR data without the IP. The following formula was used to determine which data gave the closest comparison,

$$(\text{relative error})_r(\%) = \frac{(\text{OAR}_{\text{IP},r} - \text{OAR}_{W,r})}{\text{OAR}_{W,0}} \times 100,$$

where $\text{OAR}_{\text{IP},r}$ is OAR on the IP (the phosphor layer) at r millimeters from the central axis. $\text{OAR}_{W,r}$ is OAR with the IP and the filter in r millimeters from the central axis and likewise $\text{OAR}_{W,0}$ is the one in 0 mm from central axis. Unless stated, the value for the OAR is computed with the arithmetic average of relative errors locating from -60 to -100 mm from central axis at a 10 cm depth, where the errors obviously show up, with a 10×10 cm^2 field size and 100 cm SSD.

1. Material of the filters

The materials used in this evaluation are simple substances with atomic number (Z) from 4 to 82. Concerning the material data, the simulation was carried out in two ways, one simply using the density of every material,[22] the other setting the density to the one of lead, 11.35 g/cm^3, for all the materials in order to observe the Z dependency. The thickness was fixed to 2 mm and there was no gap between the filter and the IP.

2. Filter thickness

For this evaluation, only the lead filter was used. The filter thickness was varied from 0 to 15 mm and there was no gap between the filter and IP in the calculation.

3. Filters displacement

The lead filter was also used for this calculation. The distance between the IP and the filter (expressed by "Interval" in Fig. 4) was varied from 0 to 15 mm for two cases; filter thicknesses of 2 and 1 mm. We set water equivalent data in the interval.

III. RESULTS AND DISCUSSIONS

A. MC simulation parameter settings and evaluation

As reported by Olch,[11] the dependence of the pixel value from IP measurement on dose is given in Fig. 5, and this is expressed by a logarithmic relationship. The energy spectrum used in the simulation is shown in Fig. 6. For comparison, the results of the calculation and the measured PDD and OAR are shown in Fig. 7. As can be seen in Fig. 7(a), the calculated depth dose relationship is in good agreement with the measured data. From Fig. 7(b) we can find the average values of the relative error from -60 to -100 mm from the central axis with and without the IP. These are $20.7\pm2.6\%$ for the measurement and $20.5\pm3.0\%$ for the simulation, showing good agreement for the OAR. These results infer that the MC simulation settings used were realistic.

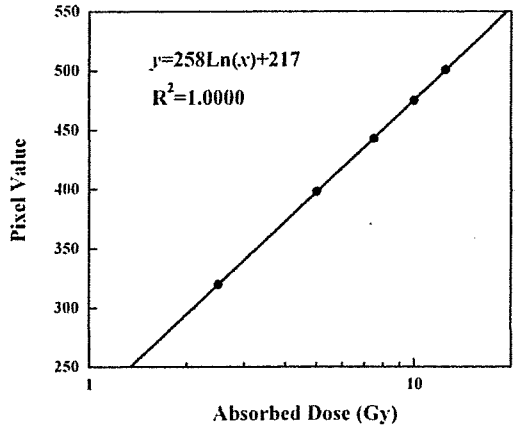

FIG. 5. Relationship between absorbed dose and pixel value along the central axis of a 10×10 cm^2 field in 10×10 mm^2.

B. Investigating the filter by MC simulation

The calculated OAR is shown in Fig. 8, which shows that, compared with the dose in water (dose with no IP in water), there is a $20.5\pm3.0\%$ difference in the average value of the relative error from -60 to -100 mm from central axis with the IP only, a $15.3\pm2.7\%$ difference for the IP with a 2 mm copper filter placed above it and a $9.8\pm2.2\%$ difference for the IP with a lead filter. It can be seen that the use of filters shifts the result closer to the dose in water with no IP.

First, we shall discuss the appropriate material to be used for the filter. A similar calculation to that shown in Fig. 8 was done for each material in order to determine the appropriate filter. The results are shown in Fig. 9. As the results show, placing a filter on each side of the IP produced a better effect than with a single filter on either side. In Fig. 9(a), compared to Ag(Z=47) and Nd(Z=60), Ba(Z=56) has a higher relative error based on t-tests ($P<0.001$). This is because Ba has a density of 3.5 g/cm^3 and thus, compared with Ag (density: 10.5 g/cm^3) and Nd (density: 6.9 g/cm^3), has a smaller ratio between density and Z. On the other hand, Fig. 9(b) shows the Z dependency only for filter materials (Z=4–82), from which we can see that the effect produced by the filter improves as Z increases, and, as the results indicate, using a high density filter material on both sides leads to a much better effect. Considering the results and the materials that are practical to use, we conclude that Pb would be the most appropriate filter material.

Our second discussion is with regard to the filter thickness. The MC simulation results are shown in Fig. 10, which

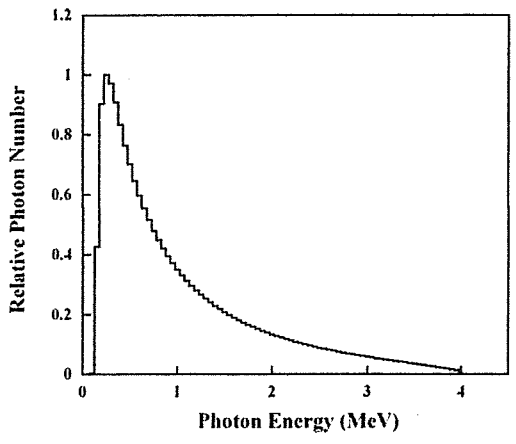

FIG. 6. Photon energy spectrum used in MC calculation.

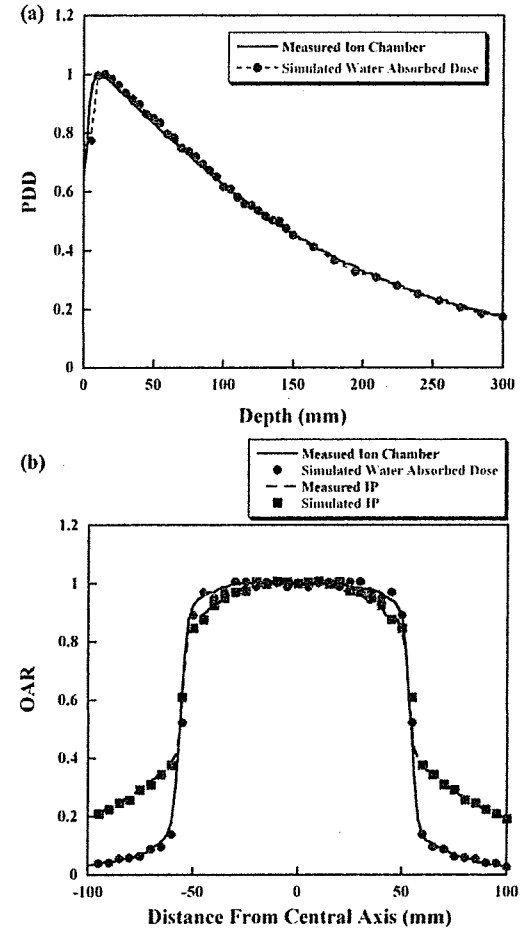

FIG. 7. Comparison of MC calculation with measurements. (a) PDD in beam axis. (b) OAR at 10 cm depth.

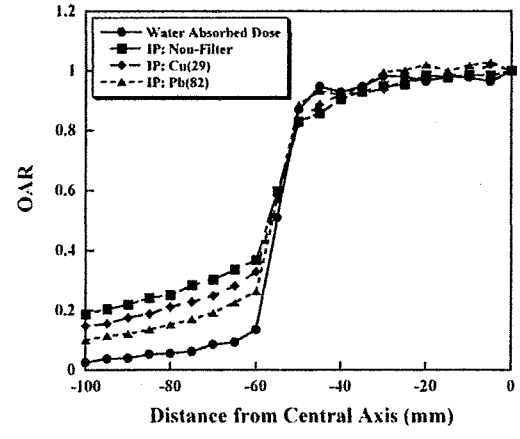

FIG. 8. Comparison of the OAR in water for nonfilter and 2 mm thick Cu and Pb filters where the filter is placed in contact with the IP.

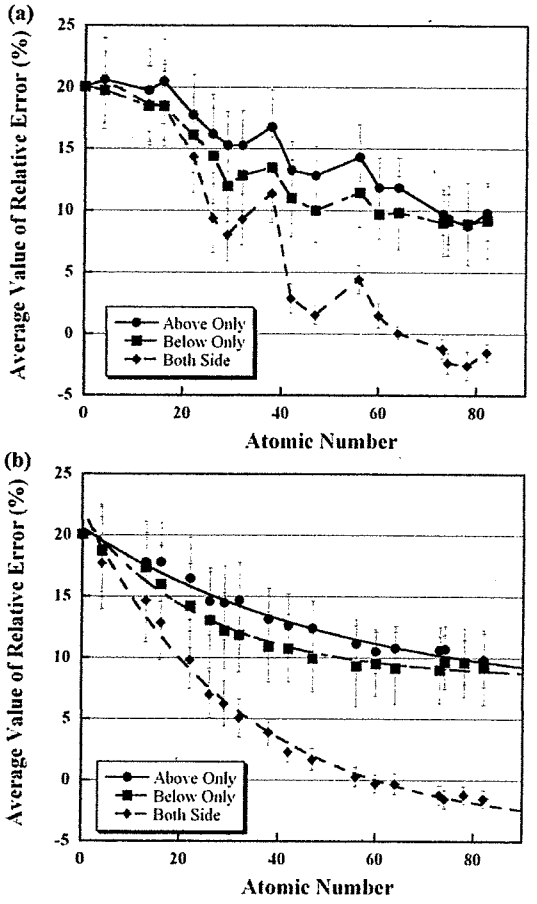

FIG. 9. Average value of relative error from −60 to −100 mm from the central axis for different filter materials. Atomic number 0 means that no filter is used. (a) Result using the density (g/cm^3) associated with each atomic number. (b) Similar to (a) but using a constant density value of 11.35 g/cm^3 for each atomic number material.

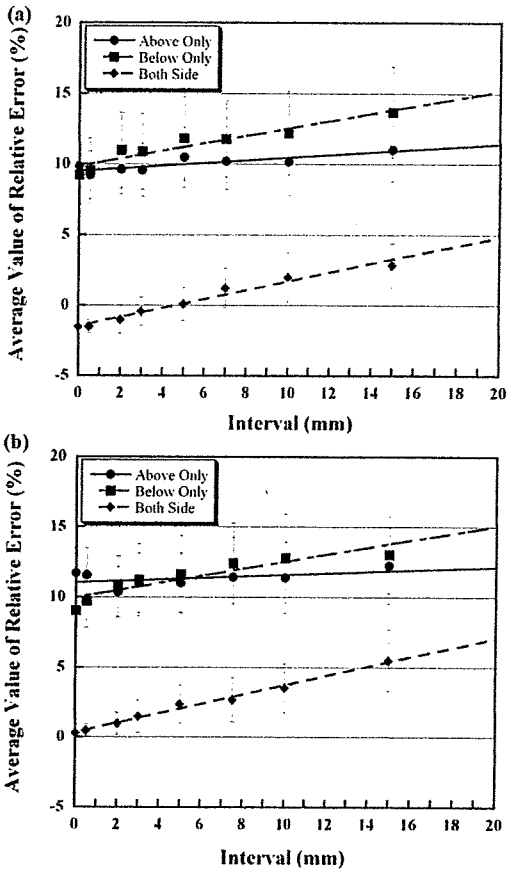

FIG. 11. Average value of relative error as a function of the distance between the filters and the IP (interval). Interval 0 means that these are in contact. (a) Average values of relative error using a 2 mm thick Pb filter. (b) Average values of relative error using a 1 mm thick Pb filter.

shows the relationship between the relative error and the thickness of the Pb filter from −60 to −100 mm from central axis. It can be seen that there is a general trend for the relative error to fall to a constant value as the filter thickness is increased. For the filter placed under the IP, this occurs for a thickness of 1 mm, and is due to the contribution of low energy photons scattered from the IP. According to the results, good agreement was found between the calculated OAR without an IP and when using 1 mm thick Pb filters on each side of the IP. If filters thicker than 1 mm are used, the effect becomes excessive. As shown in Fig. 10, the gradient of the relative error curve is steep at 1 mm, so that, when making the filter, care should be taken in the precision of the thickness; for example, if the filter were to be 0.75 or 1.5 mm in thickness, relative errors of $1.8 \pm 0.8\%$ or $-0.9 \pm 0.6\%$, respectively, would arise.

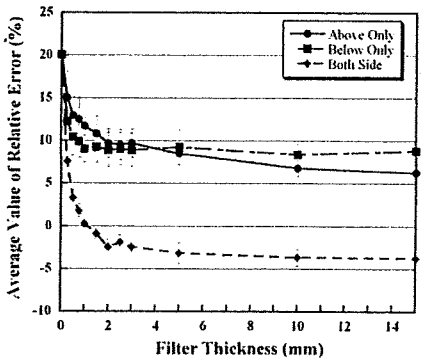

FIG. 10. Average value of relative error vs Pb filter thickness. Filter thickness 0 means no filter is used.

So far we have determined the most suitable material and the thickness of the filter. Finally, we discuss the position of the filter with respect to the IP. The relationship between the relative error and the distance of the Pb filter from the IP was calculated. Figure 11 represents the results for 2 mm thick Pb filters [Fig. 11(a)] as well as 1 mm thick filters [Fig. 11(b)]. There is no significant position dependent effect observed for the filter placed above the IP; whereas, for ones placed beneath or on both sides of the IP, the relative errors increase linearly as the distance between the IP and the filter increases. It is indicated that the filter effect tends to diminish. The scattered photons basically have a lower energy spectrum and scatter into a larger solid angle. In addition to this, since the IP includes high atomic number (Z) materials,

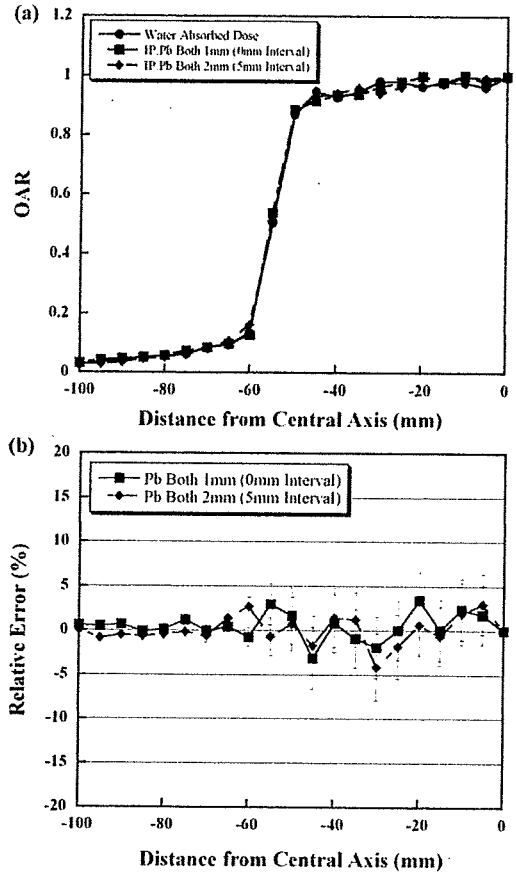

FIG. 12. (a) Comparison between the OAR calculated in water (no IP) and the OAR in water with an IP with 1 mm thick Pb filters and 2 mm thick Pb filters. (b) Relative error vs distance from the central axis.

such as Ba, the lower energy photons are attenuated much than higher ones. This is how the ratio of the energy given to IP by the backscattered photons from down stream of the IP is greater than that by photons scattered from upper stream of IP where water exist between the IP and the filter and the scatter is caused mainly by interaction with water. Therefore, the contribution to the IP of photons backscattered from under the IP is much larger than photons scattered from the upper side of the IP. This is the reason, if the interval is large, the filter position affects the relative errors. Essentially, the best options for position found from the results are with filters placed on each side of the IP, either with 2 mm Pb filters with a 5 mm interval or 1 mm Pb filters with a 0 mm interval (i.e., filters attached to both sides of the IP). Note that precision is also needed when placing the filters at the recommended distances. The OARs of the optimum filter positions and that without an IP (OAR in water) are shown in Fig. 12(a). In addition, the relative errors derived from the results in Fig. 12(a) are shown in Fig. 12(b), which showed that the relative errors of 1 mm Pb filters with a 0 mm interval and 2 mm Pb filters with a 5 mm interval distributed around 0% both in and out of the field. There was a good agreement with the result of the water absorbed dose. In detail, we calculated the root mean square of the relative error in terms of out-of-field (from −60 to −100 mm) and in-field (from

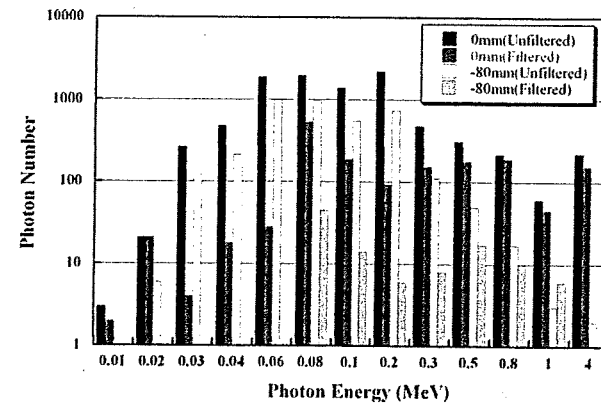

FIG. 13. Comparison of the energy spectra of photons (1×10^8 photons) interacting in the IP, on the beam axis and at −80 mm from the central axis for the cases with no filter and 1 mm thick Pb filters attached to each side of the IP.

0 to −50 mm). The results of 1 and 2 mm thick Pb filters were 2.0% and 2.0% in the field and 0.6% and 1.1% out of the field, respectively. Thus, this simulation study indicated that, by using two 1 mm thick Pb filters attached to each side of the IP or two 2 mm thick Pb filters placed 5 mm from each side of the IP, it is possible to obtain OAR curve with IP as accurate as the one based on the absorbed dose calculated only in water.

We also investigated the energy spectra in the IP with and without filters. We calculated the energy spectrum in each case from the MC analysis and the results are shown in Fig. 13. What the figure shows is that the number of photons in the low energy range (especially keV range), where there is an energy dependency on the IP, is reduced by the filter. Thus, the accuracy of the IP measurement is improved when the filter is used. The OAR measurement, in particular, can be done without concern about the energy dependency of the IP.

In study of Olch,[11] a 0.4 mm Pb filter was placed on both sides of an IP and a 6 MV photon OAR measurement was done. This is different from our study where 1 mm Pb filters were attached to both sides of the IP. What we have done in our study is completely different to his research with respect to using different IPs, energies, different procedures, and so on. To make a comparison with his study and also to develop a more reliable filter, a further more detailed study using more sophisticated calculation conditions would be needed. Additionally a certain distance of 5 mm from each side of the IP obtained in this study was suggested as one of parameters for using the Pb filters as simply as possible. This was the result that we tried to figure out some parameters as less as possible, by which it is expected that the quality assurance would be performed easily and quickly. However, it may also be important that the consideration of specific parameters suitable for each measurement condition would be needed to investigate the possibility of use of IP as a quality assurance tool with high accuracy.

[1]L. Stanton, Radiology **78**, 445 (1962).
[2]J. F. Williamson, F. M. Khan, and S. C. Sharma, Med. Phys. **8**, 94 (1981).
[3]C. W. Cheng and I. J. Das, Med. Phys. **23**, 1225 (1996).

[4]P. Cadman, Med. Phys. **25**, 1435 (1998).
[5]M. D. R. Thomas and A. P. Warrington, Phys. Med. Biol. **51**, 1439 (2006).
[6]M. Fuss, E. Sturtewagen, C. D. Wagter, and D. Georg, Phys. Med. Biol. **52**, 4211 (2007).
[7]L. J. van Battum, D. Hoffmans, H. Piersma, and S. Heukelom, Med. Phys. **35**, 704 (2008).
[8]M. Sonoda, M. Takano, J. Miyahara, and H. Kato, Radiology **148**, 833 (1983).
[9]J. A. Rowlands, Phys. Med. Biol. **47**, R123 (2002).
[10]S. M. Kengyelics, A. G. Davies, and A. R. Cowen, Med. Phys. **25**, 2163 (1998).
[11]A. J. Olch, Med. Phys. **32**, 2987 (2005).
[12]M. Homma, K. Tabushi, Y. Obata, T. Tamiya, S. Koyama, and T. Ishigaki, Jpn. J. Med. Phys. **22**, 118 (2002).
[13]H. H. Li, A. L. Gonzalez, H. Ji, and M. Duggan, Med. Phys. **34**, 103 (2007).
[14]S. E. Burch, K. J. Kearfott, J. H. Trueblood, W. C. Shiels, J. I. Yeo, and C. K. Wang, Med. Phys. **24**, 775 (1997).
[15]I. J. Yeo, C. K. Wang, and S. E. Burch, Med. Phys. **24**, 1943 (1997).
[16]S. G. Ju, Y. C. Ahn, S. J. Huh, and I. J. Yeo, Med. Phys. **29**, 351 (2002).
[17]S. Agostinelli, J. Allison, K. Amako, J. Apostolakis, H. Araujo, P. Arce, M. Asai, D. Axen, S. Banerjee, G. Barrabd, F. Behner, *et al.*, Nucl. Instrum. Methods Phys. Res. A **506**, 250 (2003).
[18]L. I. Schiff, Phys. Rev. **83**, 252 (1951).
[19]G. E. Desobry and A. L. Boyer, Med. Phys. **18**, 497 (1991).
[20]C. R. Baker, B. Ama'ee, and N. M. Spyrou, Phys. Med. Biol. **40**, 529 (1995).
[21]M. Partridge, Phys. Med. Biol. **45**, N115 (2000).
[22]S. M. Seltzer and J. H. Hubblell, *Photon Attenuation Coefficient Data Book* (Japan Society of Radiological Technology, Kyoto, 1995).

THE JOURNAL OF DERMATOLOGY

doi: 10.1111/j.1346-8138.2009.00729.x

Journal of Dermatology 2009; **36**: 663–665

LETTER TO THE EDITOR

Iatrogenic vulvar skin metastases after interstitial radiotherapy for recurrent cervical cancer

Dear Editor,

We report a case of a 68-year-old woman with iatrogenic vulva skin metastasis after interstitial radiotherapy (ISRT) was performed for recurrence in the vaginal stump of uterine cervical carcinoma. At age 65 years, she complained of atypical vaginal bleeding. The diagnosis was uterine cervical adenosquamous carcinoma with direct vaginal invasion. She received abdominal radical hysterectomy, bilateral salpingo-oophorectomy, pelvic lymphadenectomy, and para-aortic lymphadenectomy in our institution on 31 August 2006. The pathological stage was T2aN0M0. Postoperative adjuvant whole pelvic radiotherapy using four-portal box fields (50.4 Gy in 28 fractions) was performed because of deep invasion (>1/2) to the muscle layer from 21 September 2006.

On 14 August 2008, high-dose-rate ISRT was started using iridium-192 (36 Gy in six fractions twice a day for 3 successive days). A Martinez Universal Perineal Interstitial Template (MUPIT) utilizing eight metal needle applicators[1,2] with individual diameters of 1.5 mm and lengths of 160–200 mm for Micro-Selectron HDR (Chiyoda Technol, Tokyo, Japan) were used for the recurrence in the postoperative vaginal stump (Fig. 1). The external view is shown in Figure 1(a), the scout view of computed tomography in Figure 1(b), and the dose distribution in the machine for radiotherapy planning in Figure 1(c). On January 2009, multiple vulvar skin metastases were found (Fig. 2). The metastatic lesions approximated with the sites on the skin where the needle applicators had been inserted, and where she complained of pain. On 20 January 2009, a biopsy of the vulva skin was performed. The diagnosis was poorly differentiated carcinoma involving the vulva (Fig. 3a), and which was consistent with metastases from previously resected primary uterine cervical carcinoma (Fig. 3b).

Interstitial radiotherapy by MUPIT is a good choice to deliver high-dose radiation in recurrent gynecological malignancies after external beam radiotherapy where conventional brachytherapy application is not feasible and is likely to give optimal dose distribution. Furthermore, locoregional control obtained with ISRT is good and within the accepted range of complications.[3–5] This MUPIT template consists of a central large hole for placement of tandem and an array of small holes around this large hole for insertion of needles. The eight needles were inserted into the tumor and surrounding tissue and withdrawn on the final day. Uterine cervical carcinoma typically advances in a predictable fashion locally and through the lymphatic route. Lymphatic metastases usually occur first in the pelvic nodes and later in the para-aortic and/or supraclavicular nodes. In more advanced stages, the tumor cells spread hematogenously, representing lung or liver metastases. According to Sakurai *et al.*[6] in Gunma University, a total of 74 out of 256 patients (29%) between 1976 and 1994 had recurrence after definitive radiation therapy alone, and regarding first sites of recurrence, recurrent locoregional cancers were identified in 22 patients (30%), lymphogenous cancer in 22 patients (30%) and hematogenous in 19 patients (26%). Of the lymphogenous recurrences, eight (36%) developed in para-aortic nodes, 11 (50%) developed in supraclavicular nodes and three (14%) developed at both sites. Cervical cancer often spreads through direct local extension and through the lymphatics and skin. Also, cutaneous metastases from cervical cancer are very rare (i.e. <2%).[7–9] Therefore, it is considered that iatrogenic skin metastasis after ISRT occurred in this case through the same mechanism of intra- and extrahepatic disseminations of hepatocellular carcinoma after radiofrequency thermal

Correspondence: H. Yamashita, M.D., Ph.D., Department of Radiology, University of Tokyo Hospital, 7-3-1 Hongo, Bunnkyou-ku, Tokyo 113-8655, Japan. Email: yamashitah-rad@h.u-tokyo.ac.jp

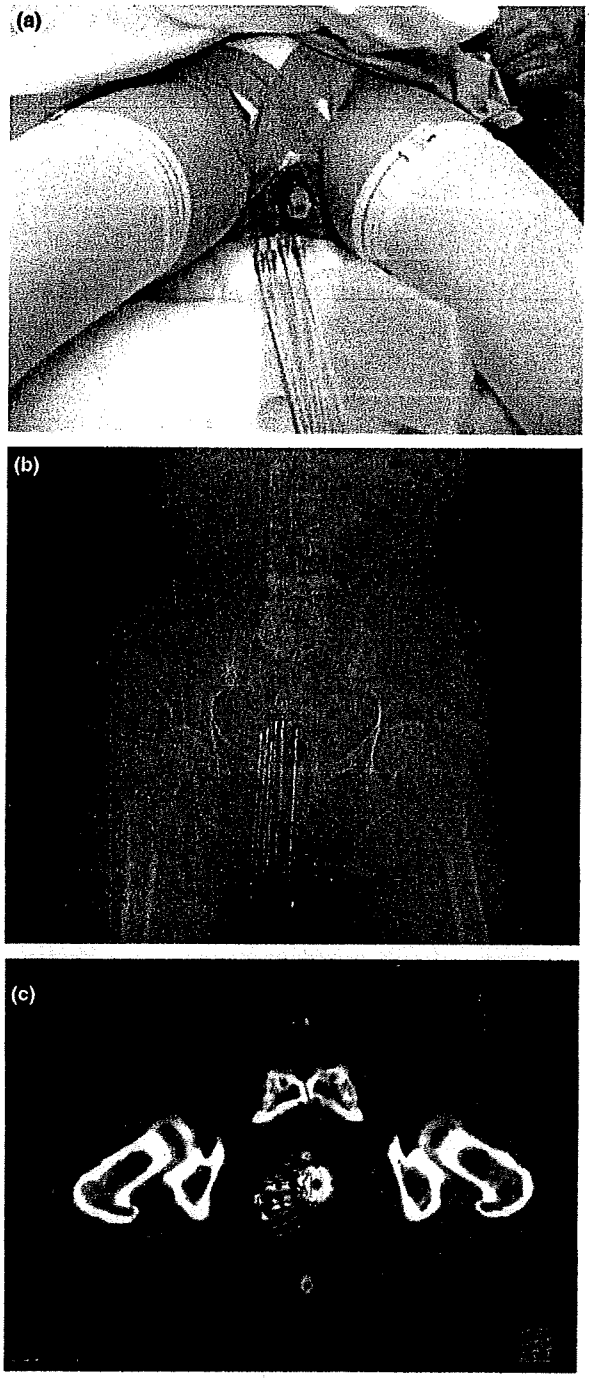

Figure 1. Interstitial radiotherapy with eight metal applicators. (a) External view; (b) scout view of computed tomography (CT); (c) dose distribution in the machine for radiotherapy planning.

Figure 2. Iatrogenic multiple vulvar skin metastases.

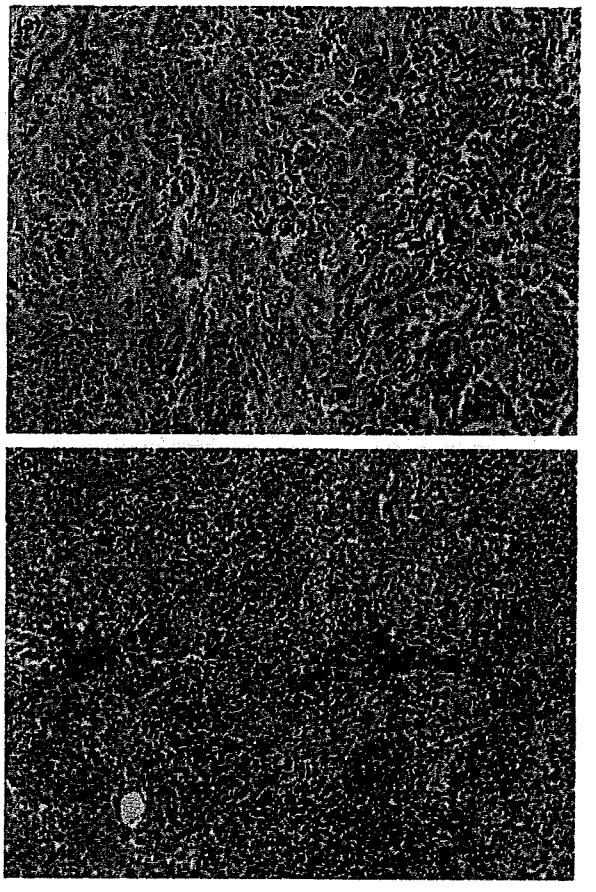

Figure 3. Hematoxylin–eosin staining. Poorly differentiated carcinoma involving (a) the vulva and (b) previously resected primary uterine cervical carcinoma (original magnifications ×100).

ablation.[10] To our knowledge, iatrogenic skin metastasis after ISRT has not been previously reported.

Hideomi YAMASHITA,
Kae OKUMA, Keiichi NAKAGAWA
Departments of Radiology, University of Tokyo Hospital, Tokyo, Japan

REFERENCES

1 Nandwani PK, Vyas RK, Neema JP, Suryanarayan UK, Bhavsar DC, Jani KR. Retrospective analysis of role of interstitial brachytherapy using template (MUPIT) in locally advanced gynecological malignancies. *J Cancer Res Ther* 2007; **3**: 111–115.
2 Martinez A, Edmundson GK, Cox RS, Gunderson LL, Howes AE. Combination of external beam irradiation and multiple-site perineal applicator (MUPIT) for treatment of locally advanced or recurrent prostatic, anorectal, and gynecologic malignancies. *Int J Radiat Oncol Biol Phys* 1985; **11**: 391–398.
3 Gupta AK, Vicini FA, Frazier AJ *et al.* Iridium-192 transperineal interstitial brachytherapy for locally advanced or recurrent gynecological malignancies. *Int J Radiat Oncol Biol Phys* 1999; **43**: 1055–1060.
4 Agrawal PP, Singhal SS, Neema JP *et al.* The role of interstitial brachytherapy using template in locally advanced gynecological malignancies. *Gynecol Oncol* 2005; **99**: 169–175.
5 Itami J, Hara R, Kozuka T *et al.* Transperineal high-dose-rate interstitial radiation therapy in the management of gynecologic malignancies. *Strahlenther Onkol* 2003; **179**: 737–741.
6 Sakurai H, Mitsuhashi N, Takahashi M *et al.* Analysis of recurrence of squamous cell carcinoma of the uterine cervix after definitive radiation therapy alone: patterns of recurrence, latent periods, and prognosis. *Int J Radiat Oncol Biol Phys* 2001; **50**: 1136–1144.
7 Imachi M, Tsukamoto N, Kinoshita S, Nakano H. Skin metastasis from carcinoma of the uterine cervix. *Gynecol Oncol* 1993; **48**: 349–354.
8 Srivastava K, Singh S, Srivastava M, Srivastava AN. Incisional skin metastasis of a squamous cell cervical carcinoma 3.5 years after radical treatment – a case report. *Int J Gynecol Cancer* 2005; **15**: 1183–1186.
9 Behtash N, Ghaemmaghami F, Yarandi F, Ardalan FA, Khanafshar N. Cutaneous metastasis from carcinoma of the cervix at the drain site. *Gynecol Oncol* 2002; **85**: 209–211.
10 Yamashita H, Nakagawa K, Shiraishi K *et al.* External beam radiotherapy to treat intra- and extra-hepatic dissemination of hepatocellular carcinoma after radiofrequency thermal ablation. *J Gastroenterol Hepatol* 2006; **21**: 1555–1560.

THE JOURNAL OF GENE MEDICINE
J Gene Med 2009; 11: 598–604.
Published online 27 April 2009 in Wiley InterScience (www.interscience.wiley.com) DOI: 10.1002/jgm.1337

RESEARCH ARTICLE

Enhanced transgene expression in the mouse skeletal muscle infected by the adeno-associated viral vector with the human elongation factor 1α promoter and a human chromatin insulator

Mayuyo Mori-Uchino[1,2†]
Takamasa Takeuchi[1†]
Isao Murakami[1,3]
Tetsu Yano[2]
Toshiharu Yasugi[2]
Yuji Taketani[2]
Keiichi Nakagawa[4]
Tadahito Kanda[1]*

[1]*Center for Pathogen Genomics, National Institute of Infectious Diseases, Tokyo, Japan*

[2]*Department of Obstetrics and Gynecology, Faculty of Medicine, The University of Tokyo, Tokyo, Japan*

[3]*Department of Obstetrics and Gynecology, School of Medicine, Keio University, Tokyo, Japan*

[4]*Department of Radiology, Graduate School of Medicine, The University of Tokyo, Tokyo, Japan*

*Correspondence to:
Tadahito Kanda, Center for Pathogen Genomics, National Institute of Infectious Diseases, 1-23-1 Toyama, Shinjuku-ku, Tokyo 162-8640, Japan.
E-mail: kanda@nih.go.jp

†Both investigators contributed equally and should be considered as senior authors.

Received: 11 September 2008
Revised: 26 January 2009
Accepted: 18 March 2009

Abstract

Background Efficient and continuous expression of a therapeutic transgene is a key factor for improving the efficacy of gene therapy. Some insulators are known to contribute to continuous high-level expression of a therapeutic transgene.

Methods Using the human AAVS1 insulator (DHS) found in the AAVS1 DNase I hypersensitive site, chicken β-globin insulator (cHS4) and sea urchin arylsufatase insulator (Ars), we newly constructed three recombinant adeno-associated virus vectors (rAAV) and examined their capability of transducing the mouse quadriceps muscle.

Results DHS increased transgene expression from the human elongation factor 1α promoter (EF) by 1000-fold, up to the high level achieved by the human cytomegalovirus immediate early promoter/enhancer (CMV), which comprises an extremely strong promoter for driving a transgene. cHS4 enhanced the expression by 100-fold, whereas Ars did not. The enhanced expression was maintained for at least 24 weeks. Vector copy numbers were similar with and without DHS or cHS4; thus, the enhancement is most likely due to up-regulated transcription. Neither DHS, nor cHS4 affected transgene expression from CMV. DHS enhanced expression from the human muscle creatine kinase promoter/enhancer by 100-fold in mice, as did DHS from EF.

Conclusions Although DHS was unable to further enhance high expression from the strong viral enhancer/promoter, it enhanced low expression from the human promoters by 100- to 1000-fold. Thus, DHS may be useful for constructing rAAVs that express a therapeutic transgene from less efficient, tissue specific promoters. Copyright © 2009 John Wiley & Sons, Ltd.

Keywords AAV vector; insulator; transduction of muscle

Introduction

Recombinant adeno-associated virus vector (rAAV), which is highly stable and can infect various organs, is considered to be suitable for *in vivo* administration in gene therapy [1,2]. Because the rAAV genome lacks the viral rep gene, whose product mediates the viral DNA replication and the integration of the viral DNA into the AAVS1 region in chromosome 19, the rAAV genome is

not replicable and does not undergo site-specific integration [3,4]. Recent studies have shown that the vast majority of infected rAAV genomes persist in the muscle in an extra-chromosomal circular form [5–7]. A variety of integration junctions between the rAAV genome and host chromosome have been recovered, indicating that a small fraction of the infected rAAV genomes is integrated at random sites [8]. The expression of transgene introduced by rAAV lasts for a long time, and some successful animal data have allowed human clinical trials to be conducted using rAAVs for the treatment of cystic fibrosis, hemophilia B, and Parkinson's disease [9–11].

Efficient and continuous expression of a therapeutic transgene is a key factor for improving the efficacy of gene therapy. Insulators comprise an element with the potential to induce continuous high-level expression of a transgene. Insulators have been shown experimentally to comprise the DNA sequences that define a domain of gene expression by directionally protecting a promoter from enhancers in different domains and by acting as a boundary to the surrounding heterochromatin [12]. Heterochromatinization is associated with silencing epigenetic modifications, including histone deacetylation and DNA methylation. Insulators appear to have mechanisms that counteract the silencing effects of heterochromatin [13,14].

In previous studies, insulators were inserted into vector genomes to protect their transgene expression cassettes from the negative influences brought about by adjacent elements. Expression of the transgene integrated in the host chromosome with a lentivirus vector carrying the chicken β-globin insulator is two-fold higher than that with the insulator-less vector [15]. The chicken β-globin insulator inserted into an adenovirus vector shields a downstream promoter from viral enhancers or silencers that are present in the vector genome [15–18].

In the present study, we constructed rAAVs with the selected insulator and injected them into the skeletal muscle of mice. Because previous studies have indicated that the great majority of rAAV genomes are maintained as extra-chromosomal concatemers, the muscle is an appropriate organ to target when aiming to avoid dilution of vector genomes by host cell division. The insertion of the insulator enhanced transgene expression from the human elongation factor 1α promoter and human muscle creatine kinase promoter/enhancer but did not affect expression from the human cytomegalovirus immediate early promoter/enhancer. These data suggest that the insulator has capacity to enhance transgene expression from a less efficient promoter.

Materials and methods

Vector plasmids

The DNA fragment encoding luciferase, which was excised from pGL4.10 (Promega Corp., Madison, WI, USA) by digestion with *Kpn*I and *Xba*I, was inserted between *Kpn*I and *Xba*I in the multiple cloning site of pEF1/Myc-HisA (Invitrogen Corp., Carlsbad, CA, USA) to yield pEF1α-luc containing a luciferase expression cassette driven by the human elongation factor 1α promoter (EF). pAAV-hrGFP (Stratagene, La Jolla, CA, USA) was digested with *Xho*I and treated by a DNA Blunting Kit (Takara-Bio Inc., Otsu, Japan), followed by further digestion with *Mlu*I, and then electrophoresed on an agarose gel. The DNA fragment containing plasmid backbone, two inverted terminal repeats (ITRs), and hGH-polyA signal (pAAV-ITR) was extracted from the gel. The luciferase expression cassette, which was excised by digestion of pEF1a-luc with *Mlu*I and *Pme*I, was ligated with pAAV-ITR to generate pAAV-EF1-Luc. pAAV-EF1-Luc was digested with *Mlu*I and treated by DNA Blunting Kit, followed by the insertion of *Bam*HI linker to add a *Bam*HI site for the insertion of the insulator fragment. The DHS-S1 region (352 bp, nucleotides 27897527–27897176 of NT_011109.15) [19] was amplified from HeLa genomic DNA by polymerase chain reaction (PCR) with a forward primer having a *Bam*HI site and a reverse primer having a *Bgl*II site, and the resultant fragment was designated as DHS. The chicken β-globin insulator core region (244 bp) [20] and the sea urchin arylsufatase insulator region (578 bp) [21] were generated by annealing of the synthetic complementary oligonucleotides with the sequences of these regions and the recognition sequences of *Bam*HI and *Bgl*II at the 5′ and 3′ ends and the resultant DNA fragments were designated as cHS4 and Ars, respectively. Stuffer, a transcriptionally inert DNA fragment, was amplified from a modified *Renilla* luciferase gene (nucleotides 1329–1679 of phRG-TK (Promega Corp.)) by PCR with a forward primer with a *Bam*HI site and a reverse primer with a *Bgl*II site. Stuffer and the insulator elements were inserted into the *Bam*HI site of pAAV-EF1-Luc to produce pAAV-EF-Stuffer, pAAV-EF-DHS, pAAV-EF-cHS4, and pAAV-EF-Ars, respectively.

A DNA fragment containing the human cytomegalovirus immediate early promoter/enhancer (CMV) and β-globin intron of pAAV-hrGFP was amplified by PCR using primers having *Hin*dIII sites at their 5′ ends. pAAV-EF-Stuffer, pAAV-EF-DHS, pAAV-EF-cHS4, and pAAV-EF-Ars were digested with *Hin*dIII to remove the promoter region (EF) and then ligated with the CMV fragment to produce pAAV-CMV-Stuffer, pAAV-CMV-DHS, pAAV-CMV-cHS4, and pAAV-CMV-Ars, respectively. The C2 site of CMV [22] was removed from pAAV-CMV-Stuffer and pAAV-CMV-DHS to produce pAAV-CMV/E(−)-Stuffer and pAAV-CMV/E(−)-DHS, respectively.

Human muscle creatine kinase enhancer and promoter regions were amplified from human keratinocyte genomic DNA by PCR with the primers for the enhancer (5′-GGATCCTCGAGCCACCCAGGGCCCCGT-3′ and 5′-CTCGAGGGAGGGTCTCGGTCGCCG-3′) and for the promoter (5′-CTCGAGGCCCAGGAAGGGCTGGTGGCTGAA-3′ and 5′-AAGCTTGGCTGGGCTGGGCTGAAGGGG-3′). After cloning the PCR-fragments into pGEM-T easy (Promega Corp.), the enhancer fragment was obtained

DOI: 10.1002/jgm

by digestion with *Bam*HI and *Xho*I and the promoter fragment was obtained by digestion with *Xho*I and *Hin*dIII. These two fragments were ligated at *Xho*I site to produce the human muscle creatine kinase promoter/enhancer (CKM) and then ligated with the larger fragment obtained by digestion of pAAV-EF1-Luc with *Bam*HI and *Hin*dIII. Stuffer and the insulator elements were inserted into the *Bam*HI site of the resulting plasmid to produce pAAV-CKM-Stuffer, pAAV-CKM-DHS, pAAV-CKM-cHS4, and pAAV-CKM-Ars, respectively.

Cells

The 293 FT cells were grown in the Dulbecco's modified Eagle's medium (Invitrogen Corp.) containing 10% fetal bovine serum, penicillin (50 μg/ml), kanamycin (100 units/ml) (growth medium) supplemented with G418 (500 μg/ml).

The C2C12 cells [23] were grown in the growth medium and passaged every other day.

rAAVs

The 293 FT cells (5×10^6) were seeded in a 10-cm poly D-lysine dish (BD Biosciences, San Jose, CA, USA) and incubated for 24 h. The cells were transfected with a mixture of a vector plasmid (3 μg) and a helper/packaging plasmid (pEEV-XX2) [24] (9 μg) by using 36 μl of Lipofectamine 2000 (Invitrogen Corp.) per dish. The medium was changed every 24 h with the growth medium supplemented with 1× non-essential amino acid (Invitrogen Corp.) twice. The cells were lysed by freeze–thaw 3 days after the transfection and rAAV was purified by the heparin affinity column method, as described previously [25].

The purified rAAV stock was treated with benzonase for 30 min at 37 °C, followed by overnight treatment of sodium dodecyl sulfate and proteinase K. Vector genome was then extracted by phenol/chloroform extraction, chloroform extraction, and ethanol precipitation. The rAAV genome copy number was measured by real-time PCR (7900HT Fast Real-Time PCR System; Applied Biosystems, Foster City, CA, USA) using Power SYBRGreen PCR Master Mix (Applied Biosystems). The PCR primers for the real-time PCR were set in the luciferase coding sequence. The forward primer was 5′-TTGTGTCCGATTCAGTCATGC-3′ (300 nM final concentration) and the reverse primer was 5′-GGTGAACATGCCGAAGCC-3′ (300 nM final concentration).

Assay of luciferase activity of C2C12 cells infected with the rAAV

The C2C12 cells (1×10^4) were seeded in a 96-well plate, incubated for 24 h, and then inoculated with the rAAV (1×10^8 genome copies). The cells were harvested at 72 h after inoculation and lysed with Passive Lysis Buffer (Promega Corp.). Luciferase activity was measured with Mithras LB940 (Berthold Technologies, Bad Wildbad, Germany) using Luciferase Assay Systems (Promega Corp.). The level of luciferase activity was exhibited in relative light units (RLU).

Assay of luciferase activity of mouse muscles injected with the rAAV

Female BALB/c mice (aged 4 weeks) purchased from Nippon SLC (Shizuoka, Japan) were used in accordance with the local institutional guidelines. The animal was anesthetized with diethyl ether and the quadriceps muscle was injected with rAAV suspended in phosphate-buffered saline (PBS) (50 μl). For comparison, some mice received plain PBS in a similar manner. The entire quadriceps muscle was removed, cut into small pieces (approximately 200 mg), and rapidly frozen on dry ice prior to luciferase analysis. The frozen muscle was mixed with passive lysis buffer with the ratio of 300 μl to 100 mg of tissue. The mixture was then homogenized with a Zirconium bead with MM300 (Retsch GmbH, Haan, Germany) at a frequency of 25 Hz for 15 min, and was left at room temperature for 15 min. The total homogenate of each leg was centrifuged at 12 000 r.p.m. (11 000 × g) for 5 min. The supernatant (20 μl) was used for the luciferase activity assay.

Assay of the vector genome copy number in the muscle

The mouse quadriceps muscle was injected with rAAV of 1×10^{10} genome copies. The muscle was isolated at 4 weeks after injection. Total DNA was extracted from the muscle by using Blood & Cell Culture DNA Midi Kit (Qiagen, Valencia, CA, USA) according to the manufacturer's instructions. The amount of the vector genome DNA in the sample was determined by TaqMan PCR. The TaqMan PCR primers and probe were set in the luciferase coding sequence. The forward primer was 5′-TTGTGTCCGATTCAGTCATGC-3′ (300 nM final concentration) and the reverse primer was 5′-GGTGAACATGCCGAAGCC-3′ (300 nM final concentration), and the probe was 5′-FAM-CTTCGGCAACCAGATCATCCCCG-TAMRA-3′ (200 nM final concentration). The TaqMan PCR conditions used were: 95 °C for 10 min, followed by 40 cycles of 95 °C for 15 s and 60 °C for 1 min in a 25-μl reaction volume. The level of vector DNA in the sample (25 ng of total muscle DNA) was estimated by comparison with the standard curve that had been produced using 1×10^1 to 1×10^5 copies of vector plasmid (coefficient of linearity ≥ 0.995). The result obtained was expressed as the rAAV DNA copy number per nucleus, assuming that one nucleus contains 6 pg of genomic DNA.

Results

Production of rAAVs with the insulator

Figure 1 shows the rAAV vector genomes constructed in the present study. We selected three insulators: DHS that had been found in a DNase I-hypersensitive site in the AAVS1 region, cHS4, and Ars, and inserted one of the insulators upstream of the promoter in the direction to insulate the luciferase expression cassette. AAVS1 on the q arm of human chromosome 19 is the specific target site of AAV2 for the integration of the viral genome. For comparison, Stuffer, an unrelated DNA fragment from the modified *Renilla* luciferase gene, was used in place of an insulator. We used four promoters: EF, CKM, CMV, and an enhancer-less version of CMV [CMV/E(−)], which lacks the enhancer region of CMV.

The rAAV was produced in the 293 FT cells transfected with the vector plasmid and the helper/packaging plasmid expressing the cap and rep genes of AAV2. The sizes of the vector genomes were in the range 3.66–4.60 kb. The rAAV was designated with the promoter and the insulator used for the construction of its vector genome. For example, rAAV having EF and DHS, CMV and cHS4, and CMV/E(−) and Stuffer were designated as rAAV-EF-DHS, rAAV-CMV-cHS4, and rAAV-CMV/E(−) -Stuffer, respectively. With our procedure, the level of each rAAV produced in a 10-cm culture plate was within the range from 3×10^8 to 5×10^8 genome copies, indicating that these insulators did not affect the packaging of the vector genome.

Transduction of mouse C2C12 cells, a myoblast cell line, with the rAAVs

The inserted DHS or cHS4 enhanced the transgene expression from EF in the C2C12 cells, a myoblast cell line derived from a C3H mouse. However, the insulators did not affect the transgene expression from CMV. The rAAV (1×10^8) was inoculated to the C2C12 cells and luciferase activity of the cell lysate was measured at 72 h after inoculation (Figure 2). The luciferase activities induced by rAAV-EF-DHS and rAAV-EF-cHS4 were two- to three-fold higher than those induced by rAAV-EF-Stuffer (Figure 2A). The luciferase activities induced by rAAV-CMV-DHS, rAAV-CMV-cHS4, and rAAV-CMV-Ars were similar to those induced by rAAV-CMV-Stuffer (Figure 2A). The luciferase activity induced by rAAV-CMV/E(−) was extremely low and was enhanced by the insertion of DHS to the level of 1:200 of rAAV-CMV-Stuffer (Figure 2B), indicating that DHS did not compensate the CMV enhancer. Thus, DHS and cHS4 raised the transgene-expression from EF to a level comparable to that induced from CMV, which is one of the most efficient promoter/enhancer systems.

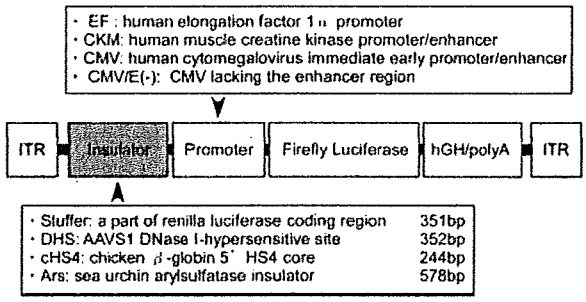

Figure 1. Schematic representation of rAAV genomes. ITR, inverted terminal repeat; hGH/pA, poly A site of human growth hormone gene

Transduction of the mouse muscle with the rAAVs

Figure 3A shows luciferase activities induced by rAAV-EFs in mice. The quadriceps muscle of 4-week-old female BALB/c mice was injected with 50 µl of the rAAV-EFs (1×10^8, 1×10^9 or 1×10^{10} genome copies) in PBS or plain PBS for the measurement of background. Each rAAV preparation was injected into five (in some cases, four or six) legs. The left and right legs were used for different rAAVs to reduce intermouse variability. The luciferase activity of the injected muscle was measured at 4 weeks after injection. Although, at a dose of 1×10^8 genome copies, luciferase activity induced by rAAV-EF-Stuffer was almost at the background level, luciferase activities induced by rAAV-EF-DHS and rAAV-EF-cHS4 were readily detectable. The luciferase levels increased depending on the doses. At all doses tested, the average

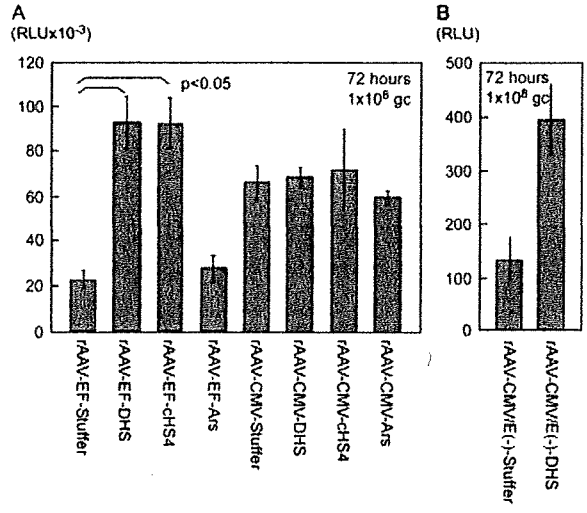

Figure 2. Transduction of C2C12 cells with (A) rAAV-EFs and rAAV-CMVs and (B) rAAV-CMV/E(−)s. C2C12 cells (1×10^4) were inoculated with the indicated rAAV and lysed 72 h later. The luciferase activity of the lysate was measured. The average of three independent experiments is presented with error bars indicating the standard deviation

DOI: 10.1002/jgm

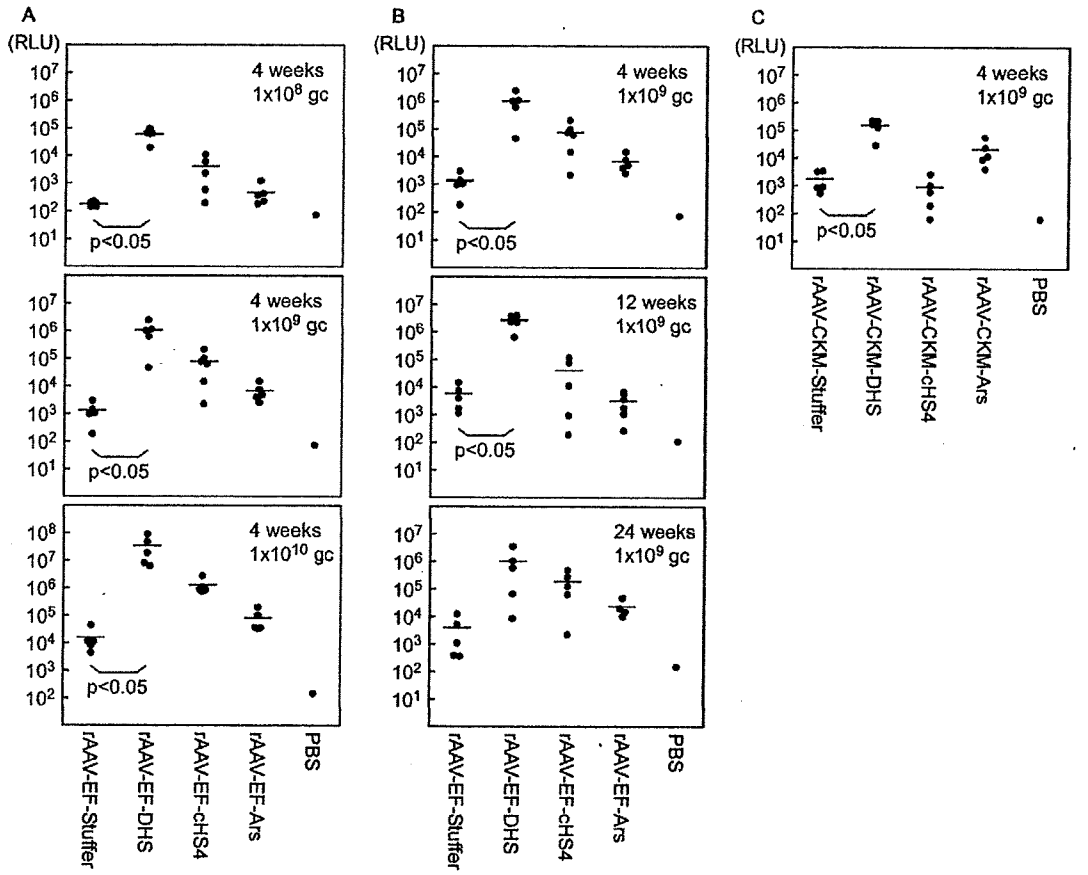

Figure 3. Transduction of the mouse muscle with rAAVs. (A) Levels of luciferase induced by various doses of rAAV-EFs. The mouse quadriceps muscle was inoculated with the indicated rAAV and harvested at 4 weeks after injection. The muscle was minced and lysed, and measured for luciferase activity. Bars indicate the average values. $p < 0.05$ (*t*-test) was considered statistically significant. (B) Levels of luciferase at 4, 12, and 24 weeks after injection with rAAV-EFs. The mouse quadriceps muscle inoculated with the indicated rAAV was harvested at 4, 12, and 24 weeks after injection. The luciferase activity was measured in a similar manner. Bars indicate the average values. $p < 0.05$ (*t*-test) was considered statistically significant. (C) Levels of luciferase induced by rAAV-CKMs. The mouse quadriceps muscle inoculated with the indicated rAAV was harvested at 4 weeks after injection. The luciferase activity was measured in a similar manner. Bars indicate the average values. $p < 0.05$ (*t*-test) was considered statistically significant

luciferase levels induced by rAAV-EF-DHS and rAAV-EF-cHS4 were 1000-fold and 100-fold higher, respectively, than that induced by rAAV-EF-Stuffer.

The luciferase activity of the mouse muscle injected with the rAAV-EFs of 1×10^9 genome copies was measured at 4, 12, and 24 weeks after injection (Figure 3B). The expression of luciferase continued for at least 24 weeks and the levels were maintained.

Figure 3C shows luciferase activities induced by rAAV-CKMs in mice. The mouse muscle was injected with one of rAAV-CKMs (1×10^9 genome copies) and luciferase activity was measured at 4 weeks after injection. The average of luciferase levels induced by rAAV-CKM-DHS was 100-fold higher than that induced by rAAV-CKM-Stuffer, indicating that DHS enhanced the transgene expression from CKM, similar to the expression from EF, in the mouse muscle.

The insulators did not affect transgene expression from CMV in the mouse muscle. The mouse muscle was injected with one of rAAV-CMVs (1×10^9 genome copies) and luciferase activity was measured at 4 weeks after injection. The luciferase level induced by rAAV-CMVs with insulator was similar to that by rAAV-CMV-Stuffer (Figure 4A). Similarly, the insulators did not affect transgene expression in the mouse muscle from the human ubiquitin C promoter, from which luciferase was induced to a level comparable to that from CMV (data not shown).

The luciferase activity of the muscle injected with rAAV-CMV/E(−)-DHS was slightly higher compared to muscle injected with rAAV-CMV/E(−)-Stuffer (Figure 4B).

To examine the transduction of tissues other than the muscle, rAAV-EFs or rAAV-CKMs (1×10^9 genome copies/250 µl of PBS) was injected to each mouse (five mice for each rAAV) through the tail vain. Because the previous study indicated that rAAVs injected through the tail vain are present mainly in the liver and spleen [24], the entire liver and spleen were harvested 4 weeks later and processed as performed for the quadriceps muscle. A low level of luciferase activity was detected only for

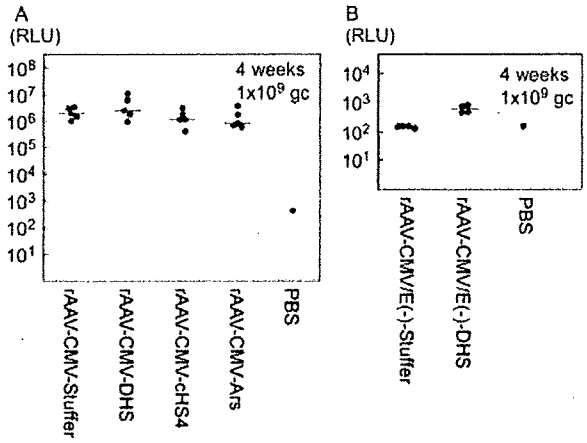

Figure 4. Transduction of the mouse muscle with (A) rAAV-CMVs and (B) rAAV-CMV/E(−) s. The mouse quadriceps muscle was inoculated with the indicated rAAV and harvested at 4 weeks after inoculation. The muscle was minced and lysed, and measured for luciferase activity. Bars indicate the average values

the liver of the mice injected with rAAV-EF-DHS (data not shown), suggesting that rAAV-EF-DHS transduced the liver more efficiently than the other rAAVs did.

Copy number of vector genome in the mouse muscle

The insulators did not affect copy number of the vector genome in the muscle. The rAAV-EFs (1×10^{10} genome copies) were injected to the quadriceps muscle in a similar manner and total DNA was extracted from the muscle at 4 weeks after injection. The level of the vector genome was measured by TaqMan PCR. Table 1 shows the calculated copy number of vector genome per nucleus. There was no significant difference between rAAV-EFs with the insulator and rAAV-EF-Stuffer. The data indicate that the enhanced luciferase activity of the muscle injected with rAAV-EF-DHS or rAAV-EF-cHS4 was not caused by a marked increase in the copy number of vector genome.

Effect of direction and location of DHS on the transduction enhancement

To determine whether or not the direction and location of DHS influence the DHS-mediated transduction enhancement, we constructed rAAV-EF-DHSs having DHS in the opposite direction or downstream of the luciferase gene and examined them for their transduction ability of mouse

Table 1. Copy number of vector genome in the mouse muscle

rAAV injected	Copy number of vector genome/nucleus	Average	SD
rAAV-EF-Stuffer	1.03, 0.76, 0.88, 0.49, 0.58	0.75	0.22
rAAV-EF-DHS	1.00, 1.16, 0.41, 2.65, 0.34	1.11	0.93
rAAV-EF-cHS4	2.39, 1.03, 7.28, 2.42, 0.84	2.79	2.62
rAAV-EF-Ars	1.75, 0.74, 0.87, 0.79, 0.22	0.87	0.55

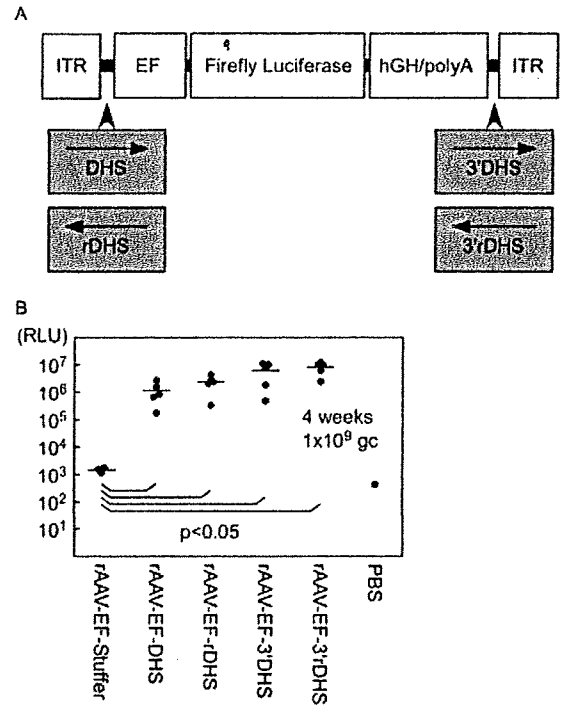

Figure 5. Transduction of the mouse muscle with rAAV-EFs having DHS in the opposite direction and downstream of the transgene. (A) Schematic representation of the various rAAV-EF-DHS genomes. ITR, inverted terminal repeat; rDHS, opposite direction to the transcription of the luciferase gene; hGH/pA, poly A site of human growth hormone gene; 3′DHS and 3′rDHS, DHS inserted downstream of the luciferase gene. (B) Levels of luciferase induced by the rAAV-EFs having DHS in the opposite direction and downstream of the transgene. The mouse quadriceps muscle was inoculated with the indicated rAAV and harvested at 4 weeks after inoculation. The muscle was minced and lysed, and measured for luciferase activity. Bars indicate the average values. $p < 0.05$ (*t*-test) was considered statistically significant

muscle. Figure 5A shows the structure of their vector genomes. The pAAV-EF1-Luc having DHS in the opposite direction was selected to produce rAAV-EF-rDHS. DHS was amplified by PCR with primers with an *Rsr*II site and inserted into the *Rsr*II site (between polyA signal and ITR) of pAAV-EF1-Luc to produce vector genomes for rAAV-EF-3′DHS and rAAV-EF-3′rDHS. These rAAVs were injected to the muscle in a similar manner, and luciferase activity of the muscle was measured 4 weeks later (Figure 5B). The luciferase activities induced by rAAV-EF-rDHS, rAAV-EF-3′DHS, and rAAV-EF-3′rDHS were comparable to that induced by rAAV-EF-DHS, indicating that the DHS-mediated enhancement does not depend on the direction or location of DHS in the AAV vector genome.

Discussion

In the present study, we newly constructed the rAAVs with selected insulators and examined their capability of transducing C2C12 cells and the mouse quadriceps

DOI: 10.1002/jgm

muscles. DHS and cHS4 raised the levels of transgene expression from EF by two- to three-fold in C2C12 cells and by 1000- and 100-fold, respectively, in the muscles. DHS also raised the levels of transgene expression from CKM by 100-fold in the muscles. Because the copy numbers of the vector genomes carrying the insulators in the mouse muscles were similar to those of the insulator-less genome, it is likely that the insulators enhanced the transcription from EF and CKM.

DHS did not enhance expression from CMV (one of the most efficient promoter/enhancer found so far) and the human ubiquitin C promoter. The data obtained suggest that DHS did not raise the presumed maximum level of transcription. Most likely, DHS enhances transcription from relatively less efficient promoters, EF and CKM. The transcriptional enhancing function of DHS, a 352 bp fragment, is likely to be useful for rAAV construction with a less efficient tissue specific promoter, such as CKM.

The molecular mechanism of the enhancement is not clear at present. Because previous studies clearly showed that the great majority of rAAV genomes are maintained as extrachromosomal concatemers of circular double-stranded DNA [5–7], DHS and cHS4 likely enhanced transcription of the transgene that was not integrated in cellular DNA. Although, in cellular DNA, the insulator sequences directionally act as boundaries to the surrounding heterochromatin that silences the genes located within [26], those in circular DNA (along with protein factors attached to DNA) may influence the entire chromatin structure of episomes. A possible structural change of the chromatin may account for the findings indicating that the insulator-mediated enhancement was independent of the direction and location of DHS in the AAV vector genome (Figure 5B). DHS inserted into the CMV/E(−) did not compensate the CMV enhancer, suggesting that the enhancing mechanism may be different from that of the classical enhancers. Further studies are required to determine how DHS enhances the transcription from the less efficient promoters.

Acknowledgements

We thank Dr Kunito Yoshiike for critical reading of the manuscript. This work was supported by Health and Labour Sciences Research Grants from the Ministry of Health, Labour and Welfare.

References

1. Flotte TR, Berns KI. Adeno-associated virus: a ubiquitous commensal of mammals. *Hum Gene Ther* 2005; **16**: 401–407.
2. Le Bec C AM. Douar AM. Gene therapy progress and prospects. Vectorology: design and production of expression cassettes in AAV vectors. *Gene Ther* 2006; **13**: 805–813.
3. Weitzman MD, Kyostio SR, Kotin RM, *et al.* Adeno-associated virus (AAV) Rep proteins mediate complex formation between AAV DNA and its integration site in human DNA. *Proc Natl Acad Sci USA* 1994; **91**: 5808–5812.
4. Giraud C, Winocour E, Berns KI. Recombinant junctions formed by site-specific integration of adeno-associated virus into an episome. *J Virol* 1995; **69**: 6917–6924.
5. Duan D, Sharma P, Yang J, *et al.* Circular intermediates of recombinant adeno-associated virus have defined structural characteristics responsible for long-term episomal persistence in muscle tissue. *J Virol* 1998; **72**: 8568–85772.
6. Vincent-Lacaze N, Snyder RO, Gluzman R, *et al.* Structure of adeno-associated virus vector DNA following transduction of the skeletal muscle. *J Virol* 1999; **73**: 1949–55.
7. Schnepp BC, Clark KR, Klemanski DL, *et al.* Genetic fate of recombinant adeno-associated virus vector genomes in muscle. *J Virol* 2003; **77**: 3495–3504.
8. Nakai H, Iwaki Y, Kay MA, *et al.* Isolation of recombinant adeno-associated virus vector-cellular DNA junctions from mouse liver. *J Virol* 1999; **73**: 5438–5447.
9. Flotte T, Carter B, Conrad C, *et al.* A phase I study of an adeno-associated virus-CFTR gene vector in adult CF patients with mild lung disease. *Hum Gene Ther* 1996; **7**: 1145–1159.
10. Kay MA, Manno CS, Ragni MV, *et al.* Evidence for gene transfer and expression of factor IX in haemophilia B patients treated with an AAV vector. *Nat Genet* 2000; **24**: 257–261.
11. Kaplitt MG, Feigin A, Tang C, *et al.* Safety and tolerability of gene therapy with an adeno-associated virus (AAV) borne GAD gene for Parkinson's disease: an open label, phase I trial. *Lancet* 2007; **369**: 2097–2105.
12. Bell AC, West AG, Felsenfeld G. Insulators and boundaries: versatile regulatory elements in the eukaryotic genome. *Science* 2001; **291**: 447–450.
13. Pikaart MJ, Recillas-Targa F, Felsenfeld G. Loss of transcriptional activity of a transgene is accompanied by DNA methylation and histone deacetylation and is prevented by insulators. *Genes Dev* 1998; **12**: 2852–2862.
14. Burgess-Beusse B, Farrell C, Gaszner M, *et al.* The insulation of genes from external enhancers and silencing chromatin. *Proc Natl Acad Sci USA* 2002; **99**(Suppl 4): 16433–16437.
15. Arumugam PI, Scholes J, Perelman N, *et al.* Improved human β-globin expression from self-inactivating lentiviral vectors carrying the chicken hypersensitive site-4 (cHS4) insulator element. *Mol Ther* 2007; **15**: 1863–1871.
16. Ma Y, Ramazani A, Lewis R, *et al.* High-level sustained transgene expression in human embryonic stem cells using lentiviral vectors. *Stem Cells* 2003; **21**: 111–117.
17. Ye X, Liang M, Meng X, *et al.* Insulation from viral transcriptional regulatory elements enables improvement to hepatoma-specific gene expression from adenovirus vectors. *Biochem Biophys Res Commun* 2003; **307**: 759–764.
18. Ramezani A, Hawley TS, Hawley RG. Performance and safety enhanced lentiviral vectors containing the human interferon-β scaffold attachment region and the chicken β-globin insulator. *Blood* 2003; **101**: 4714–4724.
19. Ogata T, Kozuka T, Kanda T. Identification of an insulator in AAVS1, a preferred region for integration of adeno-associated virus DNA. *J Virol* 2003; **77**: 9000–9007.
20. Recillas-Targa F, Pikaart MJ, Burgess-Beusse B, *et al.* Position-effect protection and enhancer blocking by the chicken β-globin insulator are separable activities. *Proc Natl Acad Sci USA* 2002; **99**: 6883–6888.
21. Akasaka K, Nishimura A, Tanaka K, *et al.* Upstream element of the sea urchin arylsulfatase gene serves as an insulator. *Cell Mol Biol* 1999; **45**: 555–565.
22. Boshart M, Weber F, Jahn G, *et al.* A very strong enhancer is located upstream of an immediate early gene of human cytomegalovirus. *Cell* 1985; **41**: 521–530.
23. Yaffe D, Saxel O. Serial passaging and differentiation of myogenic cells isolated from dystrophic mouse muscle. *Nature* 1977; **270**: 725–727.
24. Mori S, Wang L, Takeuchi T, Kanda T. Two novel adeno-associated viruses from cynomolgus monkey: pseudotyping characterization of capsid protein. *Virology* 2004; **330**: 375–383.
25. Auricchio A, Hildinger M, O'Connor E, *et al.* Isolation of highly infectious and pure adeno-associated virus type 2 vectors with a single-step gravity-flow column. *Hum Gene Ther* 2001; **12**: 71–76.
26. Burgess-Beusse B, Farrell C, Gaszner M, *et al.* The insulation of genes from external enhancers and silencing chromatin. *Proc Natl Acad Sci USA* 2002; **99**: 16433–16437.